Noninterferometric quantitative phase imaging with soft x rays

Brendan E. Allman, Phillip J. McMahon, Justine B. Tiller, Keith A. Nugent, David Paganin, and Anton Barty

School of Physics, University of Melbourne, Victoria 3010, Australia

Ian McNulty, Sean P. Frigo, Yuxin Wang, and Cornelia C. Retsch

Advanced Photon Source, Argonne National Laboratory, 9700 South Cass Avenue, Argonne, Illinois 60439

Received January 3, 2000; revised manuscript received June 6, 2000; accepted June 9, 2000

We demonstrate quantitative noninterferometric x-ray phase–amplitude measurement. We present results from two experimental geometries. The first geometry uses x rays diverging from a point source to produce high-resolution holograms of submicrometer-sized objects. The measured phase of the projected image agrees with the geometrically determined phase to within ±7%. The second geometry uses a direct imaging microscope setup that allows the formation of a magnified image with a zone-plate lens. Here a direct measure of the object phase is made and agrees with that of the magnified object to better than ±10%. In both cases the accuracy of the phase is limited by the pixel resolution. © 2000 Optical Society of America [S0740-3232(00)01710-5]

OCIS codes: 100.0100, 100.5070, 070.0070, 090.0090, 110.7440, 120.5050, 180.7460.

1. INTRODUCTION

X rays were discovered serendipitously, and their great penetrating power was confirmed by an image of the internal structure of a hand.[1] X-ray imaging has been the subject of intense development ever since. Until recently, the principal contrast mechanism was the absorption of the radiation. In medical applications, this leads to the ability to observe the projected density distribution in the object. In soft x-ray microscopy, the differential absorption contrast between oxygen and carbon is observed if radiation in the so-called water window is used.[2]

Soft x-ray microscopy with use of absorption contrast subjects the object to massive doses of radiation, leading to possible structural changes. There has therefore been considerable interest in the development of phase-contrast soft x-ray microscopy[3] that utilizes the x-ray phase contrast between elements in regions of relatively low absorption.[4,5] This work was of interest in both imaging microscopy[6] and soft x-ray holography.[7] Moreover, it can be readily observed that, away from absorption edges, the phase-contrast mechanism becomes increasingly dominant as the photon energy, E, increases (absorption contrast scales approximately as E^{-3}, while phase contrast scales as E^{-1}). For very energetic x rays, objects may show negligible absorption contrast while showing substantial phase contrast.[8]

The importance of phase-contrast mechanisms has been accentuated by the development of third-generation x-ray sources. These devices, which can produce copious quantities of coherent x rays by virtue of their very high brilliance,[9] have permitted phase-contrast imaging to become an extremely simple and standard imaging technique.[10–14] Phase-contrast tomography has also become possible.[15,16] The ideas developed in the synchrotron community have now been shown to have a role in high-brilliance laboratory sources.[12] Although these sources have a much lower brilliance than a synchrotron source, phase effects in the object can still lead to enhanced contrast and the observation of, for example, soft tissue features.

For these reasons, phase determination remains an active field of study. Early x-ray phase imaging took its lead from scanning transmission electron microscopy and utilized quadrant detectors for phase analysis.[17,18] Quadrant detectors have since been used in scanning transmission x-ray microscopy,[19] and a similar technique has been used in light microscopy.[20] A major advantage of this method is its spatial resolution, which is governed by the focal spot size of the scanning apparatus. The disadvantage is the time required to acquire a high-resolution image. Alternatively, whole image detection, for example with Shack–Hartmann arrays,[21] is instrumentally complex and provides only limited spatial phase resolution. Whole-image phase analysis in x-ray microscopy was also considered by use of Wigner deconvolution techniques. This is very computationally intensive, as it requires four-dimensional data sets.[22] Multiple defocus methods, a procedure related to that used here, have also been developed.[23,24] Various other iterative algorithms have appeared that successively approximate the phase through the development of propagated intensity between spatially separated planes.[25–27] The appeal of the method presented in the present work is that it directly (noniteratively) retrieves spatially accurate, quantitative phase by means of a computationally efficient algorithm and uses standard x-ray microscopy techniques. Moreover, existing techniques frequently intermix phase with absorption contrast. In this paper we explore the ability

to measure phase quantitatively and separate it out from the absorption contrast in the sample. The deterministic phase-retrieval technique of this paper uses the transport of intensity approach,[28,29] which has been used elsewhere,[30] though a flexible solution procedure is a more recent development.[31] This work is an extension of our earlier experimental[8] and theoretical[32] work in which the absorption had to be minimized for phase recovery.

We begin in Section 2 with a brief review of our theoretical approach. In Section 3 we go on to describe our experimental arrangement. We consider two experimental configurations. The first one that we describe is a holographic setup in which our test objects are illuminated from a diverging point source, the focus of a zone plate. These results are presented in Section 4. An alternative arrangement that will permit phase information to be obtained is that of an imaging microscope.[33] We present results from this configuration in Section 5. In Section 6 we draw together our results and conclude the paper.

2. THEORETICAL BASIS FOR THE PHASE RECOVERY

The flow of optical energy must obey the continuity equation for energy conservation to be obeyed. For a time-invariant, statically stationary coherent wave the continuity equation has the form,

$$\nabla \cdot [I(\mathbf{r})\nabla\phi(\mathbf{r})] = 0, \tag{1}$$

where $I(\mathbf{r})$ is the probability density and $\phi(\mathbf{r})$ is the phase of the x radiation. With an appropriately defined phase,[31] Eq. (1) is also valid for partially coherent radiation. It can be shown that, under most conditions, this equation may be uniquely solved for the phase, given a knowledge of the three-dimensional intensity. In other words, the intensity and phase are coupled in a unique manner, and knowledge of one determines the other. A concrete example of this is the action of a perfectly transmitting lens. The lens changes the phase of the incident wave, but not its amplitude, with the consequent change in intensity distribution as the light is focused upon further propagation. The direction of propagation is perpendicular to the wave (phase) front.

In the case of an x-ray synchrotron beam, the direction of propagation of the radiation is at only a small angle to the average beam direction. That is, it satisfies the paraxial approximation.[34] In this case, Eq. (1) may be rewritten in the form of the so-called transport of intensity equation (TIE),[28,29]

$$k\frac{\partial I(\mathbf{r})}{\partial z} = -\nabla_\perp \cdot [I(\mathbf{r})\nabla_\perp\phi(\mathbf{r})], \tag{2}$$

for a wave $\sqrt{I(\mathbf{r})}\exp[i\phi(\mathbf{r})]$, with irradiance $I(\mathbf{r})$ and phase $\phi(\mathbf{r})$. Here, $\mathbf{r} = \mathbf{r}_\perp + \mathbf{z}$, where $\mathbf{z}$ is the longitudinal optic axis and $\mathbf{r}_\perp$ ($=\mathbf{x} + \mathbf{y}$) is the plane normal to the optic axis, so that the gradient operator $\nabla_\perp$ acts in the plane of $\mathbf{r}_\perp$, k is the wave number, and $\partial I(\mathbf{r})/\partial z$ is the longitudinal intensity derivative. In the paraxial case, if the intensity and its longitudinal derivative are known over a plane, the phase of the wave in that plane can be found without recourse to interferometry.

Although we have assumed paraxial propagation in obtaining Eq. (2), we note that it also holds for a spherical incident wave under a suitable scaling of variables.[35]

The noninterferometric, propagation-based phase-retrieval procedure with the TIE has already been successfully applied to visible light,[33] x rays,[8] and electrons.[36] Our previous work in the x-ray regime assumed that the absorption was negligible. In this paper we extend this work to a range of new geometries and to objects that display substantial absorption.

In particular, we consider two distinct arrangements. The first we term holographic geometry, wherein soft x rays diverge from a diffraction-limited zone-plate focus. The diverging radiation is then used to image micrometer-sized objects with high magnification. The second geometry uses a zone-plate lens to form a magnified image of the object from which the phase and amplitude are retrieved in what we term imaging geometry. In each case, the accuracy of the phase retrieved is determined by the accuracy to which the experimental dimensions are known.

Before describing in detail the experiments and the results, we describe the beam line used in these experiments.

3. SOFT X-RAY BEAM LINE

The experimental results presented in this paper were obtained at Sector 2 Insertion Device Branch Beamline (known as 2-ID-B) at the Advanced Photon Source, Argonne National Laboratory. The beamline forms part of the Synchrotron Radiation Instrumentation—Collaborative Access Team (known as SRI-CAT) and is operated as a zone-plate microfocus source devoted to high-resolution imaging, coherent scattering, and interference studies with soft x rays.[37]

The undulator source provides a coherent flux 10^{10}–10^{12} photons/s/0.1% BW) of x rays in the range of 0.5–7.0 keV. A series of slits, multilayer mirrors, and a spherical grating monochromator selects a collimated, monochromatic (10^2–10^4 $E/\mathrm{d}E$), 1.5 mm^2 × 0.5 mm^2 (FWHM) beam of x rays in the range 0.5–4.0 keV and directs them onto a zone plate some 60 m downstream from the undulator source.

With 1.8-keV x rays, the 90-μm diameter, 110-nm-thick Ni zone plate with an outer zone width of 45 nm results in a 2.5% efficient first-order focal beam waist of 60 nm at the microprobe focus approximately 6 mm from the zone plate.

In the work described here, we use this beam line for the two separate configurations. One uses the zone plate to produce a sharp pointlike source of light, and the second uses the zone plate as an objective lens in a simple single-lens microscope.

4. HOLOGRAPHIC MICROSCOPY

A. Experimental Setup

In the first experiment the zone-plate focus is simply used as a 60-nm real point source of x rays. The geometry is

that of Gabor in-line holography,[38] but with point-source illumination and is shown in Fig. 1. This geometry retains the aberration-free imaging system (not requiring objective lenses) of in-line holography, but in a magnifying mode. We term this projection-imaging-geometry holographic microscopy.[39]

In the experiment, a collimated beam of 1.83 keV (0.682 nm) x rays is focused by the zone plate to a point 5.978 mm downstream of the zone plate. A 5-μm order-sorting aperture is placed within a few hundred micrometers of the focal spot to collect the first-order flux and remove that of higher focal orders, as well as to cut down on the direct (zeroth-order) incident beam flux.

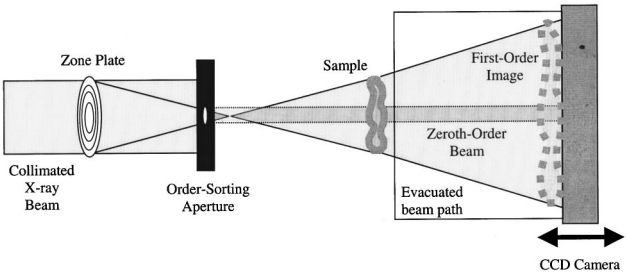

Fig. 1. Schematic of the point-source-projection, holographic geometry, noninterferometric phase-imaging experiment. The zone plate forms a first-order focus approximately 6 mm downstream. A 5-μm order-sorting aperture placed just before the focus masks other focal orders. The focus acts as a real point source and illuminates the sample placed less than 2 mm away. The projected image is detected by the CCD 530 mm further downstream. Images in closely spaced planes are taken by translating the CCD along the beam axis.

The sample, mounted on a rotation stage and a series of translation stages, is centered in the beam 1–2 mm downstream from the zone-plate focus. X rays diverge from the focus, through the sample, and enter an evacuated beam path (to minimize beam absorption); then they are detected by a soft x-ray CCD camera a further 500 mm downstream of the sample.

The CCD is thinned and backside-illuminated, with 1024×1024 pixels, each of which is 24 μm square. The focus-CCD to focus-sample distance ratio allows projection magnifications of up to 500$\times$ and spatial resolution down to 50 nm. The CCD sits on a translation stage oriented longitudinally along the propagation axis, and moving the camera permits the acquisition of intensity images in three closely spaced planes.

In the experiment, intensity images were taken at 5-mm intervals in a range of up to 40 mm so that the intensity difference could be optimized over a range of separations. The middle (in-focus) image of the set of three projected images represents the intensity distribution $I_0(\mathbf{r})$ for which the phase is being sought. The intensity difference between the outer bracketing pair of (defocused) images is used to approximate the intensity derivative, $\partial I(\mathbf{r})/\partial z$. Numerical inversion of the TIE [Eq. (2)] then provides the required phase.

The flux in the zeroth-order beam is four orders of magnitude times greater than the first-order focused beam selected by the order-sorting aperture, and so a "finger"

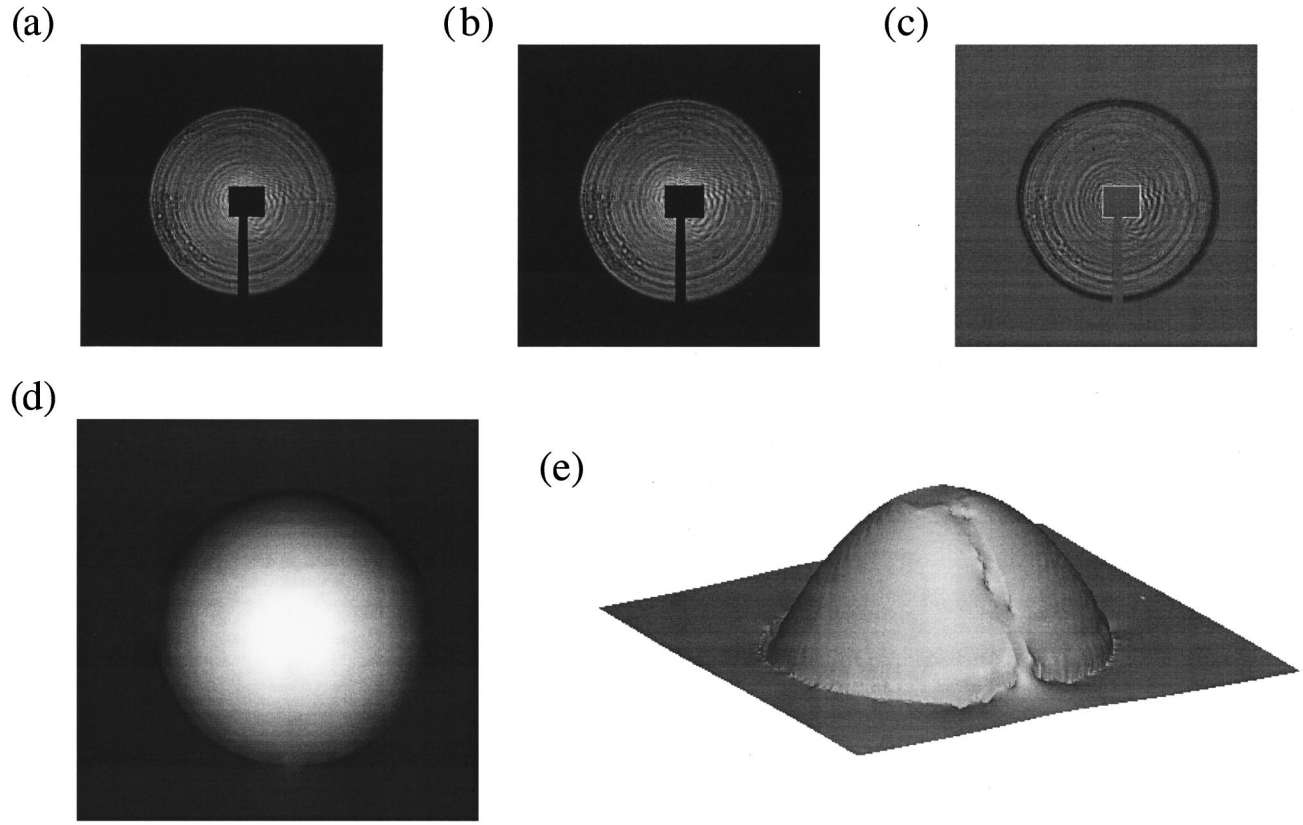

Fig. 2. Holographic geometry images of the aligned flat-field (sample-free) intensity distribution: (a) under-focused and (b) (magnified) over-focused intensity distribution, (c) intensity difference, (d) retrieved phase, and (e) rendered surface plot of the retrieved phase.

beam stop at the CCD is used to mask the direct beam intensity. Even with the beam stop, the intensity of the zeroth-order beam is still sufficiently high at the beam stop edges to cause "blooming" (overflow of charge into neighboring wells) on the CCD array. This overflow has spurious effects on the intensity distribution and hence on the intensity derivative and ultimately on the retrieved phase and so is later further masked in software. Another reason for masking the direct beam in software is that the direct and the first-order beams expand at different rates. Consequently, the direct beam adds intensity to proportionally smaller areas of the first-order distribution as the propagation distance increases and would therefore represent a conflicting flow of optical energy to the expanding first-order beam. An example of the zone-plate defocused intensity distribution is shown in Fig. 2(a). The "finger" beam stop is seen entering the circular distribution from the bottom, and the rectangular mask added in software to remove the zeroth order and intensity blooming is seen at the center of the distribution.

B. Experimental Results

The wave-front incident on the sample will clearly contain some residual phase distortions from the experimental apparatus. To examine these effects, it is important that we characterize the incident beam. As a test of our approach, we retrieved the phase of a nominally spherical wave front. To do this, we take advantage of the fact that the incident beam will be essentially spherical in form, with a radius of curvature determined by the geometry of the experiment. Figures 2(a) and 2(b) show a pair of 512×512-pixel projected intensity distributions at distances of 510 and 550 mm from the point source. Owing to the spherical wave front, they are different sizes at the CCD, a difference made obvious by the dark border to the intensity difference [Fig. 2(c)].

With the TIE, a spherical phase front was retrieved [Figs. 2(d) and 2(e)]. The recovered phase excursion across the spherical distribution is 1.60×10^5 rad. Geometrically, the expected phase excursion is $1.53 \pm 0.06 \times 10^5$ rad; the 4% error is due to uncertainties in length measurements and lateral misalignment between the two images used for the intensity difference. A circular

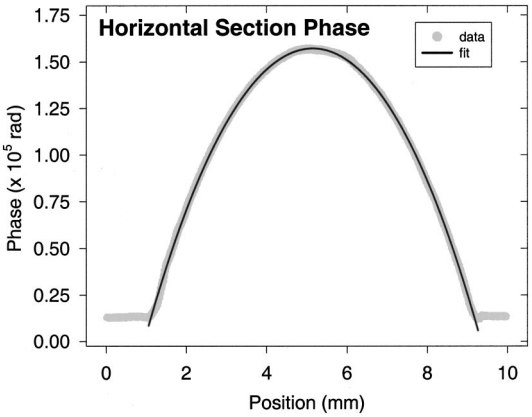

Fig. 3. Profile through the spherical phase distribution (points), with circular fit (solid curve).

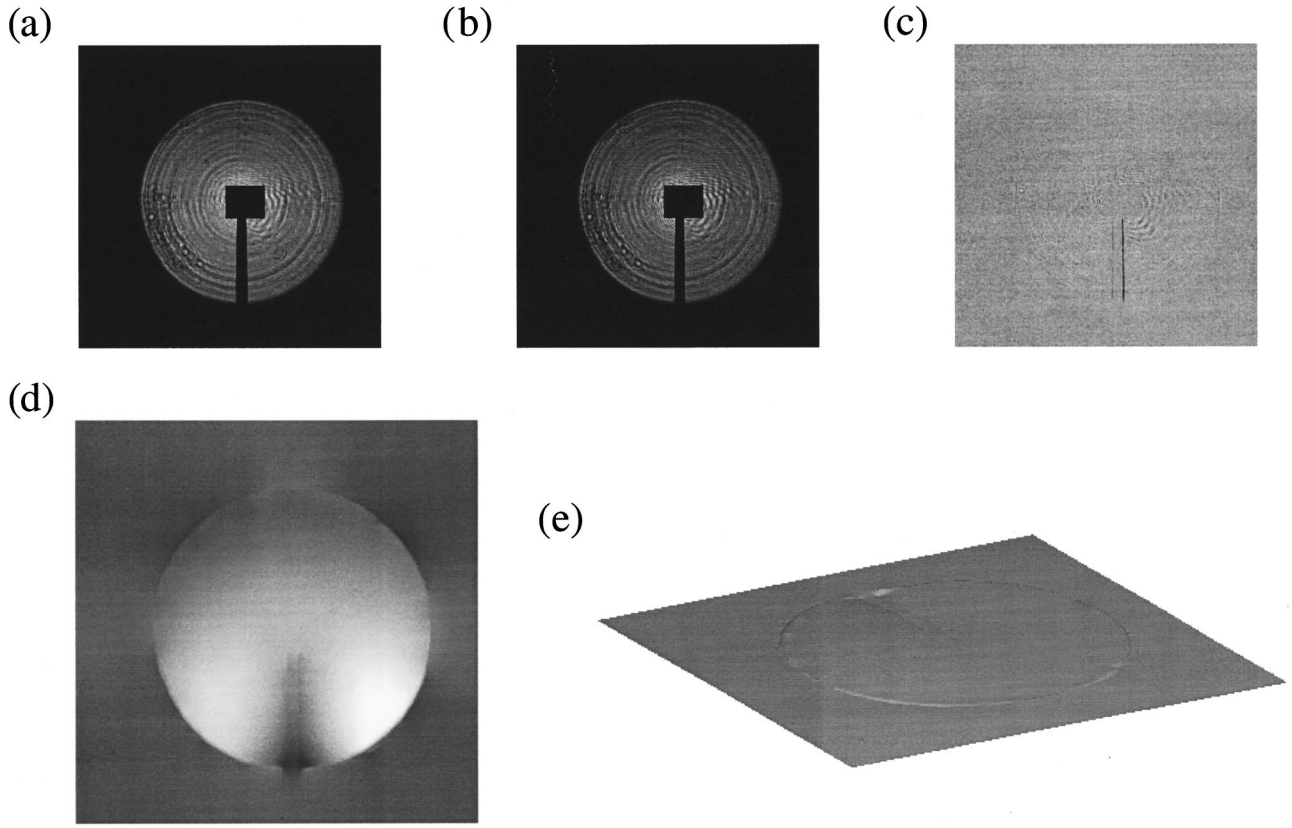

Fig. 4. Holographic geometry images of the scaled and aligned flat-field (sample-free) intensity distribution: (a) (scaled) under-focused and (b) over-focused intensity distribution, (c) intensity difference, (d) retrieved phase, and (e) rendered surface plot of the retrieved phase.

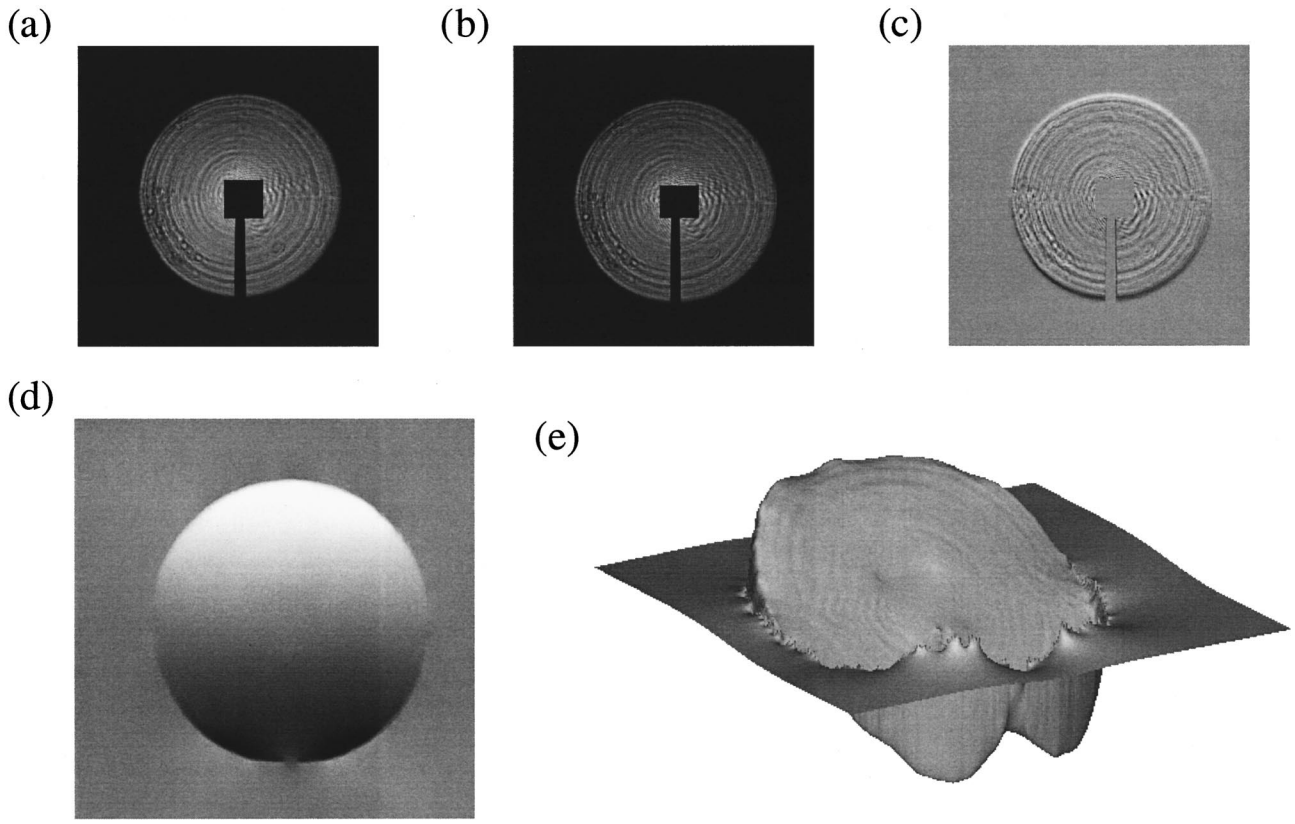

Fig. 5. Holographic geometry images of the scaled and misaligned flat-field (sample-free) intensity distribution: (a) (vertically shifted) under-focused and (b) over-focused intensity distribution, (c) intensity difference, (d) retrieved phase, and (e) rendered surface plot of the retrieved phase.

fit to a profile through this phase front is shown in Fig. 3, indicating excellent sphericity of the correct magnitude and thus quantitative phase recovery.

Scaling the two images to the same size with image processing software is equivalent to the use of collimated illumination (as in previous experiments[8,33,36]) and consequently removes the wave-front sphericity from the recovered phase signal. An example of this process is seen in Fig. 4. Figure 4(a) is Fig. 2(a) scaled to the size of Fig. 2(b) [in this case, Fig. 4(b)]. This leaves the beam stop as the most notable feature of the intensity derivative [Fig. 4(c)]. The retrieved phase distribution is relatively flat, as seen in Figs. 4(d) and 4(e). The rendered surface of Fig. 4(e) has been plotted to the same scale as that of Fig. 2(e).

Besides the spherical phase front that is due to expansion, there is phase (wave-front) tilt that reflects a transverse motion of the wave field. Therefore any misalignment between the outer image pair, due, say, to lateral motion of the CCD when translated longitudinally, is retrieved as a tilt in the phase image. As an example, the consequence of a lateral misalignment is shown in Fig. 5. In this case Fig. 5(a) has been deliberately shifted up by 10 pixels (240 μm) from Fig. 2(b) [= Fig. 5(b)], which gives a shadowed effect to the intensity derivative [Fig. 5(c)]. The resultant tilt added to the phase is shown in Figs. 5(d) and 5(e). Again, the rendered surface of Fig. 5(e) is plotted on the same scale as Fig. 2(e) for comparison.

From these sample-free images, the obvious first step in performing the phase retrieval involves optimizing the scaling and alignment of the three images (in software) to remove spherical and tilt phase artifacts from the desired phase effects of the sample. Next, to limit the effects of the zeroth-order intensity (as discussed above), it is masked out in software. The additional air path for the longer propagation distances leads to extra absorption, independent of the sample; so to ensure conservation of flux, the three images are normalized to the same integrated flux. The appropriate (also normalized) flat-field intensity distribution (a sample-free image taken with the same experimental conditions) is then divided, or equivalently subtracted in the case of intensities with small fluctuations, from each of the bracketing images. This step removes any phase structure of the illuminating beam itself. Finally, we emphasize that the solution to Eq. (2) does not require that the sample be nonabsorbing. As an alternative to aligning all three projected intensity images with the inherent scaling and alignment errors, the intensity distribution in the central plane is approximated as the average of the two bracketing images. This is advantageous for weak phase objects, for which alignment phase effects can dominate the sample phase effects.

The experimental optimization of the phase-retrieval procedure is sample dependent, as it depends most strongly on the phase gradient in the sample. The systematic phase errors introduced by incorrect scaling and alignment may be determined geometrically, and the statistical accuracy is determined by count rates. Therefore, in the absence of knowledge about the object, the

data are best collected over a range of separations and exposure times. This is the approach used in this work.

We illustrate the quantitative nature of the phase-retrieval process, this time by considering the retrieved phase of micrometer-sized aluminum spheres. A projected intensity distribution of four approximately 2-μm aluminum spheres is shown in Fig. 6(a). The shadows cast by the balls indicate considerable absorption (95%) at their centers. The light–dark border at the edge of each sphere represents the transverse flow of optical energy from the dark regions to light regions, indicative of phase effects (diffraction) from the spheres. Also visible in the image is a vertical fold in the substrate (100 nm of formvar), which displays phase distortion but minimal absorption. The corresponding flat-field (sample-free) distribution is seen in Fig. 6(b), and, to highlight the effects of the sample on the illumination, their difference is shown in Fig. 6(c).

Unfortunately, the microspheres moved relative to each other during the sequence of exposures, which meant that we could align only to an individual sphere of the set. This unwanted motion was attributed to Coulomb repulsion between the spheres. Originally, the spheres were fixed electrostatically to the insulating formvar substrate, but the passage of the intense, soft x-ray beam generated further charge on the microspheres, increasing their repulsion and eventually leading to motion.

In this instance, alignment (to fractional pixel resolution) was performed around the aluminum microsphere

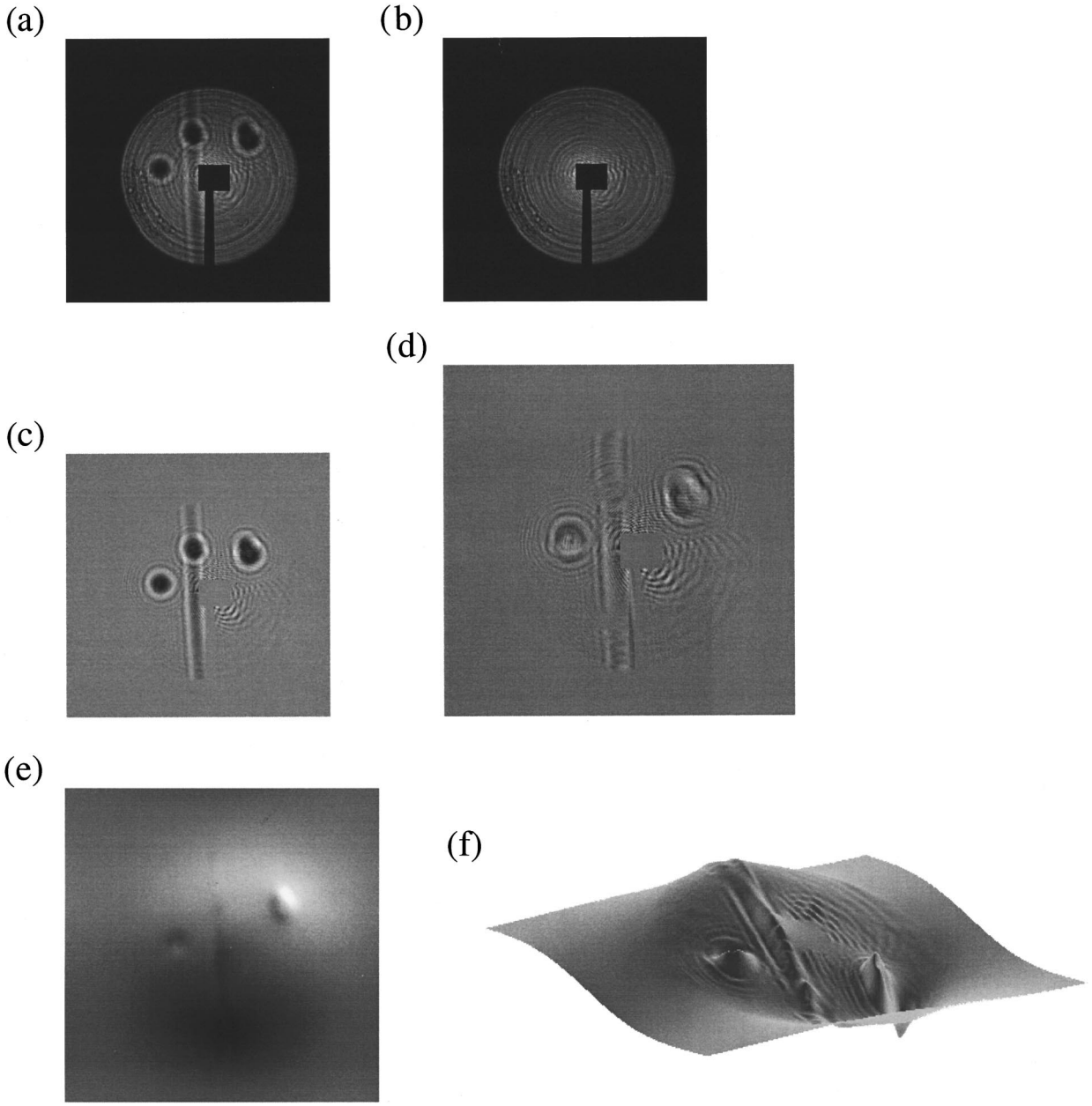

Fig. 6. Holographic geometry images of aluminum microspheres, scaled and aligned: (a) in-focus with microspheres and (b) in-focus flat-field intensity distribution, (c) intensity distribution flat-field subtracted, (d) intensity difference between defocused images, (e) retrieved phase, and (f) rendered surface plot of the retrieved phase.

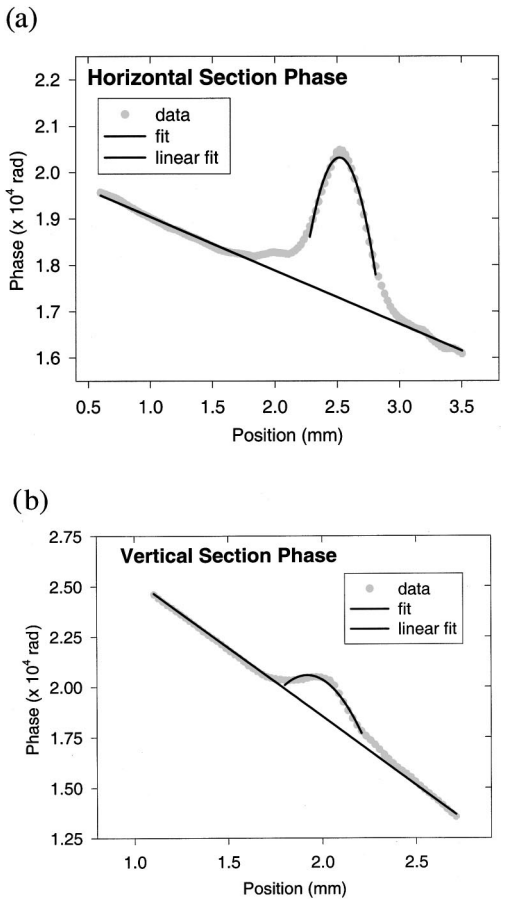

Fig. 7. (a) Horizontal and (b) vertical profiles through the phase images of the aluminum balls. The solid line and curve represent a linear fit to the phase tilt and a circular fit to the ball and indicate highly spherical phase objects. The phase effects of the fold in the substrate can be seen in the horizontal profile.

on the fold to achieve the intensity difference shown in Fig. 6(d). The effect of the aligned sphere on the intensity derivative is minimal, while large intensity oscillations are seen for the others. Such large oscillations indicate large relative misalignment between these balls and appear as large phase tilts in the retrieved phase [Fig. 6(e)]. In contrast, the aligned ball is barely discernible in the phase distribution. Horizontal and vertical profiles through the retrieved phase distribution of the aligned ball are shown in Figs. 7(a) and 7(b), respectively. The phase distribution of the aluminum ball appears on a tilted phase background owing to the misalignment of the background illumination, that is, owing to the relative motion of the sample and the illuminating beam. The effects of the fold in the formvar can be seen as additional phase structure in the horizontal phase profile. Fits to these profiles, after removal of the phase tilt, indicate a spherical phase excursion of 1900 ± 100 rad over a disturbance of radius 0.45 ± 0.05 mm. Geometrically, this corresponds to a diameter of 1.7 ± 0.5 μm at the sample plane. If the sphere is considered as a point source of spherical waves 528 mm from the CCD, then the phase excursion across the spherical phase front in the imaging plane is 1770 ± 200 rad, in agreement with the retrieved phase.

The phase so retrieved represents the phase in the image plane and not the phase at the sample position. This is an important point. To retrieve the phase (of the sample) back at the sample plane, the intensity and phase from the image plane must be backpropagated (in software) to the sample plane by use of the Fresnel (or equivalent) propagator (diffraction integral). This procedure has been implemented[40] and represents a solution to the twin-image problem in holography.[41]

5. IMAGING GEOMETRY

There exist major drawbacks with projection-geometry holographic microscopy. First, while it does allow phase retrieval in a plane downstream of the sample, this phase must then be backpropagated to the sample plane to achieve the phase map of the actual sample. Second, the presence of the zeroth-order beam contaminates the detected illumination and hence the retrieved phase. And, third, the different image sizes collected over the range of longitudinal translations led to a spherical wave front (background phase) in the retrieved phase.

To circumvent these problems, we performed a second set of phase-retrieval experiments in imaging geometry, wherein the zone-plate lens was used to form an in-focus, real, magnified image of the object. This meant that the phase retrieved in the plane of the focused image is the phase of the image, a magnified version of the actual object, and therefore requires no backprojection. Additionally, this geometry removed the zeroth-order beam from the image and eliminated any need for rescaling due to different image sizes, as will now be discussed.

A. Experimental Setup

The imaging setup contains many of the same elements as in projection mode, and a schematic is shown in Fig. 8. In this case, the sample is illuminated by a collimated, 1.83-keV x-ray beam from a 20-μm pinhole, with both the pinhole and the sample being placed upstream of the zone plate. The 20-μm beam of x rays strikes the zone plate off axis so that when the first-order, real image is formed at the CCD, it lies outside the zeroth-order beam, as seen

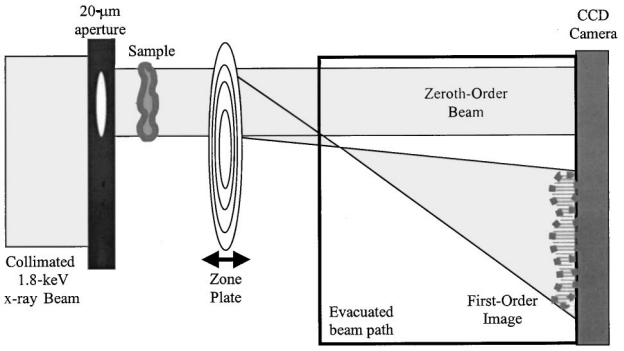

Fig. 8. Schematic of the imaging geometry, noninterferometric phase-retrieval experiment. A 20-μm aperture (defining the beam dimensions) and the sample are placed upstream of the zone plate and off center to its axis. An in-focus image of the sample that is clear of the zeroth-order beam is formed at the CCD 980 mm further downstream. Images in closely spaced planes are achieved by translating the zone plate along the beam axis.

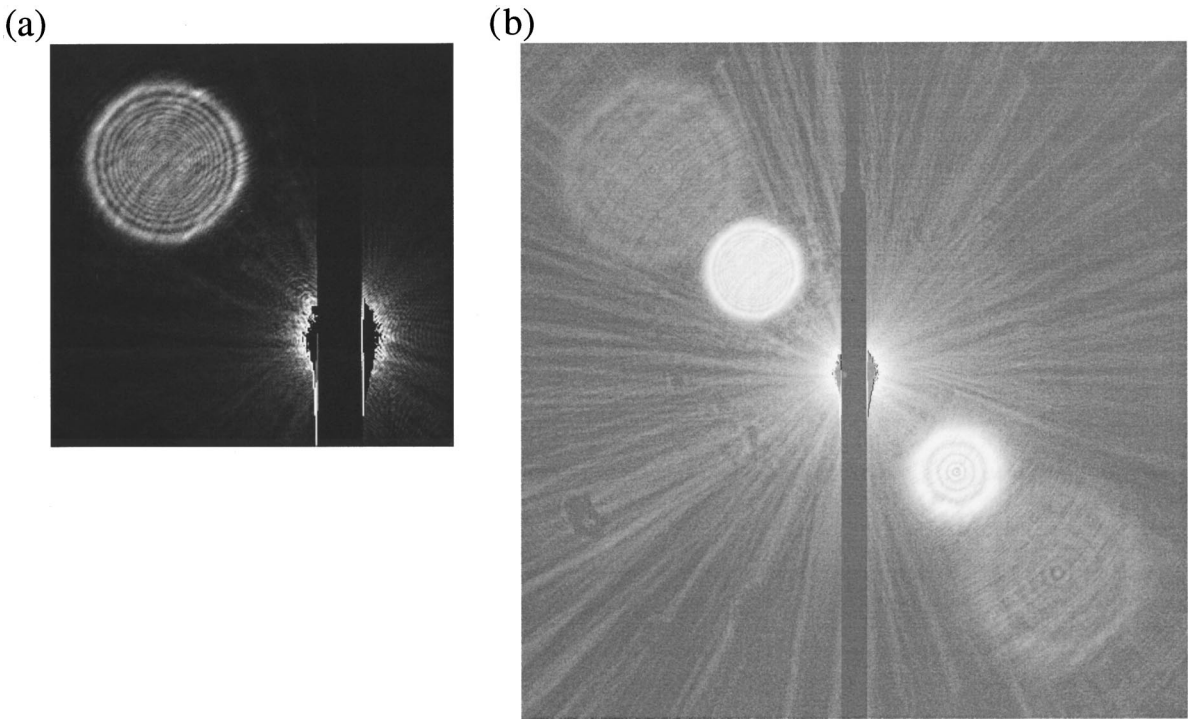

Fig. 9. Flat-field intensity distribution in imaging geometry. (a) The in-focus first-order image is seen to be well clear of the zeroth-order direct beam. (b) A logarithmic scale image is displayed that shows the central zeroth-order beam and beam stop, the in-focus +1 and out-of-focus +2 orders (upper left), and the out-of-focus −1 and −2 orders (lower right).

in Fig. 8. The lateral offset of the image is less than 1% of the propagation distance. Under these paraxial conditions, image aberrations are minimal.

An image of the first-order illuminating beam, free of any zeroth-order contamination and beam stop, is shown in Fig. 9(a). The most notable feature of the image is the diffraction rings of the aperture, indicating good coherence properties from the synchrotron source and conditioning optics. The circular arcs that appear in the images are artifacts of the zone-plate structure. In fact, the larger, logarithmic-scale image shown in Fig. 9(b) displays the central zeroth-order beam, beam stop, and higher-order beams. The in-focus +1 and out-of-focus +2 order images are to the upper left, and the out-of-focus −1 and −2 order images are to the lower right of the image. To maximize magnification, the CCD (with a longer evacuated path) is now placed further downstream (980 mm) from the zone plate. Placing the sample just outside the (upstream) focal length of the zone plate forms a magnified real image on the 256×256-pixel CCD. When the single-lens formula was applied to this geometry, magnifications of 164× were possible. We note, given the CCD pixel size, that this limited the resolution of the system to 146 nm, which is somewhat less than the resolution of the zone plate.

In this geometry, the three closely spaced images were achieved by translations of the zone plate along the beam (optic) axis. It is important to note that translating the zone plate left the alignment of the sample and beam-defining aperture fixed. Once again for experimental optimization of the intensity difference, the zone plate was translated in steps of 50–100 μm over a range of 0.5–2 mm, with a longitudinal translation stage. These small intervals meant that there was only a 0.2% change in size of the imaged intensity at the CCD. This effectively eliminated any spherical background phase contamination. However, translating the zone plate also inadvertently shifted it transverse to the beam axis, thereby introducing a phase tilt to the circular arcs of the zone plate within the illuminated region, even though the boundary to the region and sample remained fixed with respect to each other.

B. Experimental Results

As a standard phase object for calibration purposes, the 2-μm aluminum spheres were imaged first. The images (over-focused, in-focus, and under-focused) in the three closely spaced planes are shown in Figs. 10(a), 10(b), and 10(c), respectively. The same analysis procedure is followed as before, whereby the images are aligned and the effects of the illuminating intensity are removed (sample-free image subtracted) in calculating the intensity difference of the outer pair [Fig. 10(d)]. The retrieved phase is given in Figs. 10(e) and 10(f). Removal of the background phase with a high-pass filter qualitatively improves the prominence of the microspheres, as seen in Fig. 10(g) [plotted to the same scale as Fig. 10(f)].

The size of the aluminum sphere shadow (85% absorption) in Fig. 10(b) in the image plane is 360 ± 24 μm, corresponding to 2.2 ± 0.1-μm objects. At 1.83-keV x-ray energy, a thickness of 4.574 μm of aluminum is required to achieve a 2π-phase shift. Accordingly, the aluminum microspheres should have a phase excursion of 3.0 ± 0.2 rad. The retrieved phase, after being scaled by the longitudinal magnification m_L ($=m_T^2$, transverse magnification squared), has an excursion of 3.1 ± 0.5

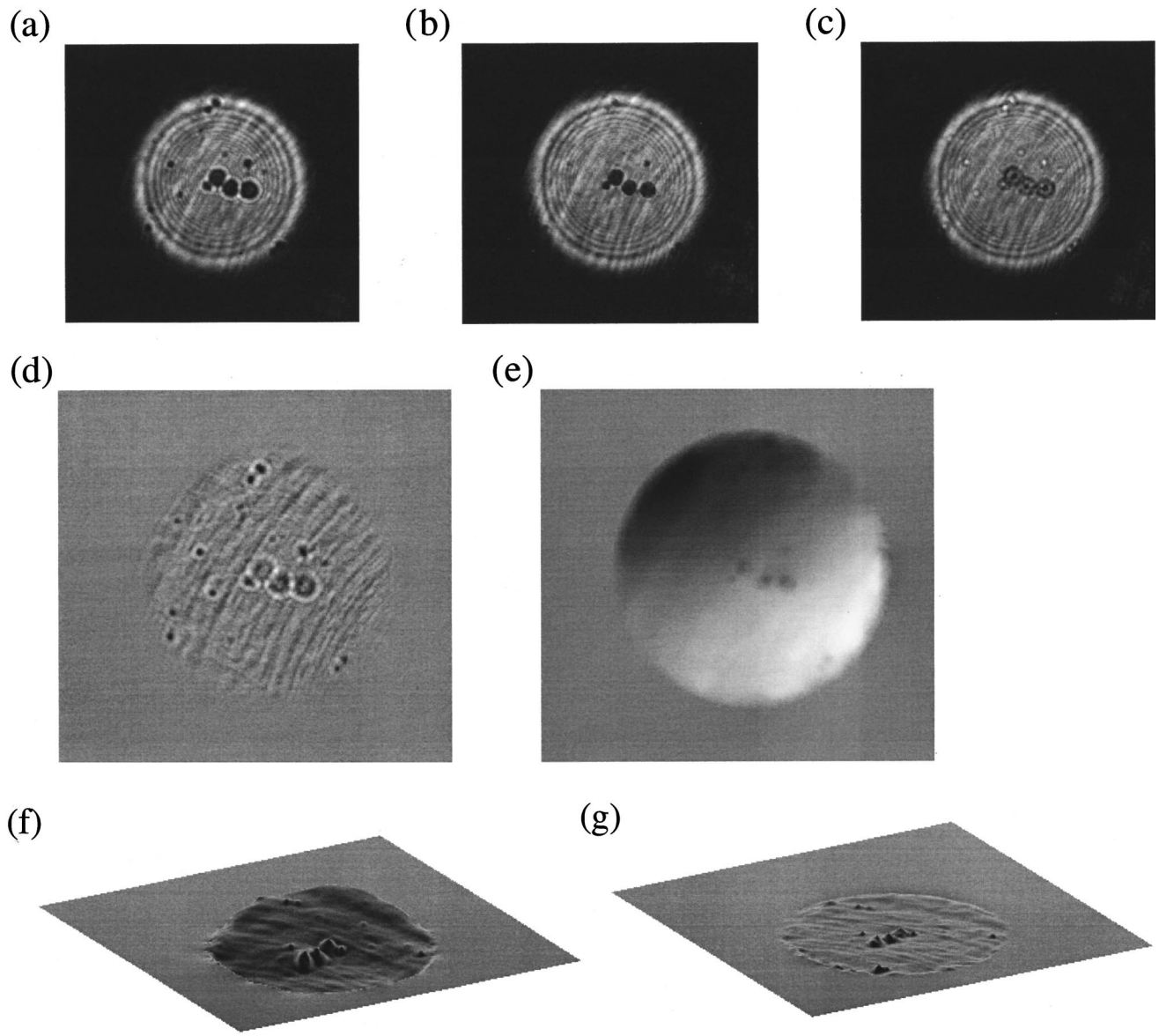

Fig. 10. Imaging geometry phase retrieval. (a) Under-focus, (b) in-focus, and (c) over-focus intensity images for the aluminum microspheres sample. (d) The intensity difference is used to retrieve (e) the phase and (f) rendered view. (g) A high-pass filter highlights the spheres while removing the low-frequency background signal.

rad, in excellent quantitative agreement with the known result. A vertical profile through the retrieved phase distribution of the middle microsphere of the three is shown in Fig. 11. The phase distribution of the sphere again appears on a tilted phase background owing to the misalignment of the illuminating beam. A circular fit to the profile, after removal of the phase tilt, indicates a spherical phase distribution, as expected.

Examples of phase retrieved from other samples, in a similar manner, were a curved section of a polycarbonate optical fiber and a length of spider web silk, shown in the image series of Figs. 12 and 13, respectively. In each case, the sequence of images displayed is the three closely spaced intensity images, the intensity difference, the retrieved phase, and the rendered phase, labeled (a) through (f), respectively. The optical fiber is ~20% absorbing and has been cropped to remove as much beam-

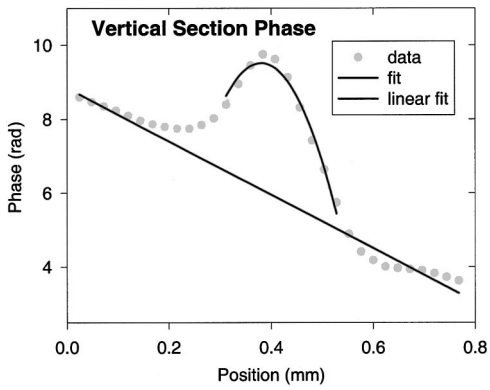

Fig. 11. Vertical profile through the phase image of the middle aluminum sphere of the three. The solid line and curve represent a linear fit to the phase tilt and a circular fit to the sphere and indicate a highly spherical phase object.

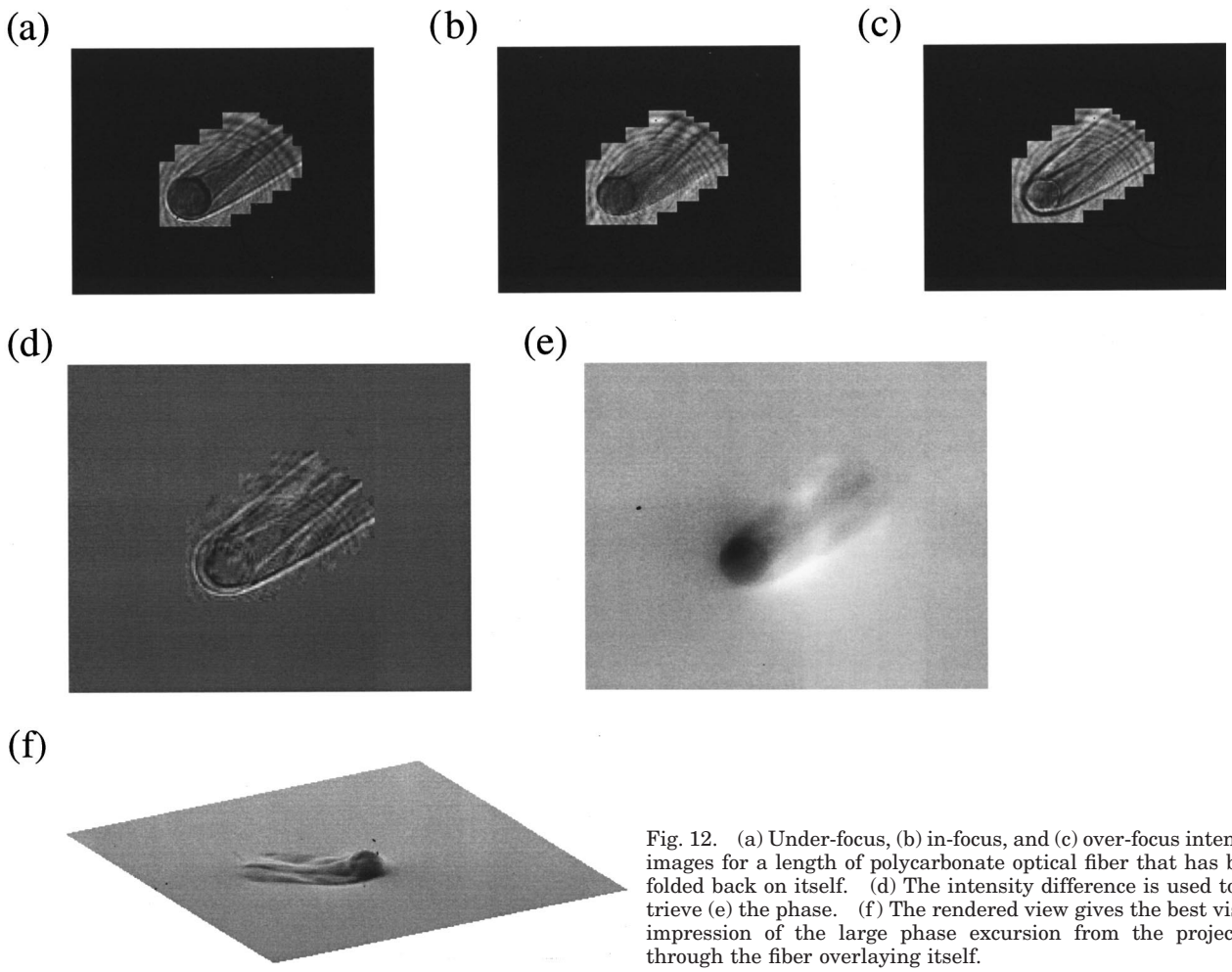

Fig. 12. (a) Under-focus, (b) in-focus, and (c) over-focus intensity images for a length of polycarbonate optical fiber that has been folded back on itself. (d) The intensity difference is used to retrieve (e) the phase. (f) The rendered view gives the best visual impression of the large phase excursion from the projection through the fiber overlaying itself.

phase artifact as possible. Approximating the (undoped) polycarbonate fiber by a carbon cylinder of the same diameter (3.70 ± 0.15 μm), we expect a phase excursion of 4.95 ± 0.20 rad. The phase retrieved for the optical fiber is 4.4 ± 0.6 rad. The length of spider web silk is 1.76 ± 0.15 μm in diameter, and, again approximating this as a carbon cylinder, its phase excursion is 2.35 ± 0.20 rad. The retrieved phase is 2.5 ± 0.4 rad, again in excellent agreement.

6. DISCUSSION AND CONCLUSION

In this paper we have described quantitative x-ray phase–amplitude imaging with two different geometries: holographic microscopy and imaging microscopy. The first of these showed, in principal, better resolution and will be of most utility where imaging geometries are not possible, such as with hard x radiation. However, this approach is able to recover the phase and amplitude only in the plane of observation; a true image of the object itself will be more difficult and will require the development of robust numerical wave-propagation procedures. This is the subject of ongoing work. The second geometry used an imaging microscope and is rather better suited to direct imaging problems. However, the resolution will not always be as high as is possible with the projection approach.

Both of the experimental configurations used here showed excellent quantitative agreement between the retrieved and the actual (estimated) phase excursion of the samples tested. Many of the measurements presented here are simply not possible with alternative approaches. For example, phase measurements are conventionally performed with interferometry. However, it is difficult to make very-high-resolution phase measurements at these wavelengths, particularly if the phase shifts are varying very rapidly over short-distance scales such as was the case, for example, with the spherical wave.

In summary, we have shown that propagation-based, noninterferometric phase retrieval allows the simultaneous collection of x-ray intensity and phase information. We have used two geometries to provide sample magnifications in the range of 150–500 times, achieving quantitative intensity and phase images with resolution near the 50-nm diffraction limit of the zone-plate lens used. It is hoped therefore that the techniques demonstrated here will find utility in a range of applications in materials science and biology.

ACKNOWLEDGMENTS

This work was performed with support from the Australian Research Council Large Grant, Fellowship and Postgraduate Award schemes, and ASRP 98/99 Proposals

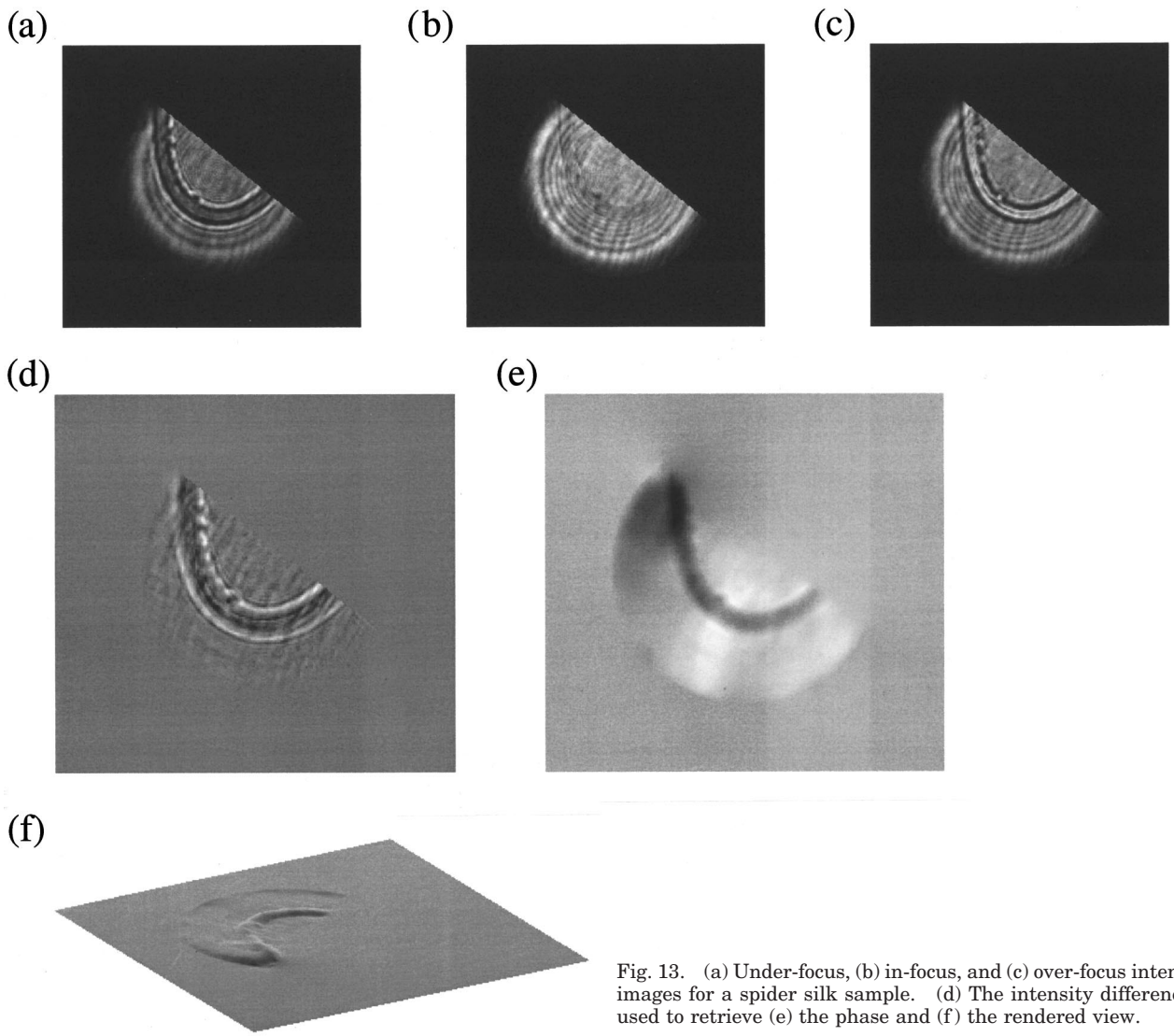

Fig. 13. (a) Under-focus, (b) in-focus, and (c) over-focus intensity images for a spider silk sample. (d) The intensity difference is used to retrieve (e) the phase and (f) the rendered view.

SRI-20 and SRI-32. We are grateful to E. Anderson for providing the zone-plate lenses. This work was supported by the U.S. Department of Energy, Basic Energy Sciences, Office of Energy Research, under contract W-31-109-ENG-38.

Brendan E. Allman can be reached at the address on the title page, by telephone at 61-3-83447403, or by fax at 61-3-93474783, or by e-mail at bea @tauon.ph.unimelb.edu.au.

REFERENCES

1. W. C. Röntgen, "On a new kind of rays," Nature **53**, 274–276 (1896).
2. B. X. Yang, J. Kirz, and T. K. Sham, "Oxygen *K*-edge extended x-ray-absorption fine-structure studies of molecules containing oxygen and carbon atoms," Phys. Rev. A **36**, 4298–4310 (1987); J. Kirz, C. Jacobsen, and M. Howells, "Soft x-ray microscopes and their biological applications," Q. Rev. Biophys. **28**, 33–130 (1995).
3. G. Schmahl, D. Rudolf, and P. Guttmann, "Phase contrast x-ray microscopy experiments at the BESSY storage ring," in *X-Ray Microscopy II*, D. Sayre, M. Howells, J. Kirz, and H. Rarback, eds., Vol. 56 of Springer Series in Optical Science (Springer-Verlag, Berlin, 1988), pp. 228–232; G. Schmahl, D. Rudolph, G. Schneider, P. Guttman, and B. Niemann, "Phase contrast x-ray microscopy studies," Optik (Stuttgart), **97**, 181–182 (1994).
4. J. E. Trebes, S. B. Brown, E. M. Campbell, D. L. Matthews, D. G. Nilson, G. F. Stone, and D. A. Whelan, "Demonstration of x-ray holography with an x-ray laser," Science **238**, 517–519 (1987); J. E. Trebes, K. A. Nugent, S. Mrowka, R. A. London, T. W. Barbee, M. R. Carter, J. A. Koch, B. J. MacGowan, D. L. Matthews, L. B. DaSilva, G. F. Stone, and M. D. Feit, "Measurement of the spatial coherence of a soft-x-ray laser," Phys. Rev. Lett. **68**, 588–591 (1992); K. A. Nugent and J. E. Trebes, "Coherence measurement technique for short-wavelength light source," Rev. Sci. Instrum. **63**, 2146–2151 (1992).
5. K. A. Nugent, "Signal to noise ratio in soft x-ray holography," J. Mod. Opt. **38**, 553 (1991).
6. G. Schmahl, P. Guttmann, G. Schneider, B. Niemann, C. David, T. Wilhein, J. Thieme, and D. Rudolph, "Phase contrast studies of hydrated specimens with the x-ray microscope at BESSY," in *X-Ray Microscopy IV*, A. Erko and V. Aristov, eds. (Bogorodski Pechatnik, Chernogolovka, Moscow Region, 1994), pp. 196–206.
7. C. Jacobsen, M. Howells, J. Kirz, and S. Rothman, "X-ray holographic microscopy using photoresist," J. Opt. Soc. Am. A **7**, 1847–1861 (1990).
8. K. A. Nugent, T. E. Gureyev, D. Cookson, D. Paganin, and

Z. Barnea, "Quantitative phase imaging using hard x-rays," Phys. Rev. Lett. **77**, 2961–2964 (1996).
9. See, for example, Advanced Photon Source, http://aps.anl.gov; European Synchrotron Radiation Facility, http://www.esrf.fr; Super Photon Ring, http://www.spring8.or.jp.
10. E. Forster, K. Goetz, and P. Zaumseil, "Double crystal diffractometry for the characterization of targets for laser-fusion experiments," Krist. Tech. **15**, 937–945 (1980).
11. T. J. Davis, T. E. Gureyev, D. Gao, A. W. Stevenson, and S. W. Wilkins, "X-ray image contrast from a simple phase object," Phys. Rev. Lett. **74**, 3173–3176 (1995); T. J. Davis, D. Gao, T. E. Gureyev, A. W. Stevenson, and S. W. Wilkins, "Phase-contrast imaging of weakly absorbing materials using hard x-rays," Nature **373**, 595–598 (1995).
12. S. W. Wilkins, T. E. Gureyev, D. Gao, A. Pogany, and A. W. Stevenson, "Phase-contrast imaging using polychromatic hard x-rays," Nature **384**, 335–338 (1996).
13. A. Snigirev, I. Snigireva, V. Kohn, S. Kuznetsov, and I. Schelokov, "On the possibilities of x-ray phase contrast microimaging by coherent high-energy synchrotron radiation," Rev. Sci. Instrum. **66**, 5486–5492 (1995).
14. P. Cloetens, R. Barrett, J. Baruchel, J.-P. Guigay, and M. Schlenker, "Phase objects in synchrotron radiation hard x-ray imaging," J. Phys. D **29**, 133–146 (1996).
15. A. Momose, T. Takeda, and Y. Itai, "Phase-contrast x-ray computed tomography for observing biological specimens and organic materials," Rev. Sci. Instrum. **66**, 1434–1436 (1995); A. Momose, T. Takeda, Y. Itai, and K. Hirano, "Phase-contrast x-ray microtomography: application to human cancerous tissues," in *X-Ray Microscopy and Spectromicroscopy*, J. Thieme, G. Schmahl, D. Rudolph, and E. Umbach, eds. (Springer-Verlag, Berlin, 1998), pp. II-207–II-211.
16. P. Cloetens, M. Pateyron-Salomé, J.-Y. Buffière, G. Peix, J. Baruchel, F. Peyrin, and M. Schlenker, "Observation of microstructure and damage in materials by phase sensitive radiography and tomography," J. Appl. Phys. **81**, 5878–5886 (1997).
17. H. Rose, "Nonstandard imaging methods in electron microscopy," Ultramicroscopy **2**, 251–267 (1977).
18. E. M. Waddel and J. N. Chapman, "Linear imaging of strong phase objects using asymmetrical detectors in STEM," Optik (Stuttgart) **54**, 83–96 (1979).
19. G. R. Morrison, A. R. Hare, and R. E. Burge, "Transmission microscopy with soft x-rays," in *Proceedings of the Institute of Physics Electron Microscopy and Analysis Group Conference* (Institute of Physics, Bristol, UK, 1987), pp. 333–336.
20. T. Wilson, A. R. Carlini, and C. J. R. Sheppard, "Phase contrast microscopy by nearly full illumination," Optik (Stuttgart) **70**, 166–169 (1985).
21. R. G. Lane and M. Tallon, "Wave-front reconstruction using a Shack–Hartmann sensor," Appl. Opt. **31**, 6902–6908 (1992).
22. H. N. Chapman, "Phase-retrieval x-ray microscopy by Wigner-distribution deconvolution," Ultramicroscopy **66**, 153–172 (1996).
23. P. Schiske, "Image processing using additional statistical information about the object," in *Image Processing and Computer-Aided Design in Electron Optics*, P. W. Hawkes, ed. (Academic, New York, 1973), p. 82.
24. W. Coene, G. Janssen, M. Op de Beeck, and D. Van Dyck, "Phase retrieval through focus variation for ultra-resolution in field-emission transmission electron microscopy," Phys. Rev. Lett. **69**, 3743–3746 (1992).
25. F. Roddier and C. Roddier, "Wave-front reconstruction using iterative Fourier transforms," Appl. Opt. **30**, 1325–1327 (1991).
26. V. Yu Ivanov, V. P. Sivokon, and M. A. Vorontsov, "Phase retrieval from a set of intensity measurements," J. Opt. Soc. Am. A **9**, 1515–1524 (1992).
27. P. Cloetens, W. Ludwig, J. Baruchel, D. Van Dyck, J. Van Landuyt, J. P. Guigay, and M. Schlenker, "Holotomography: quantitative phase tomography with micrometer resolution using hard synchrotron radiation x-rays," Appl. Phys. Lett. **75**, 2912–2914 (1999).
28. M. R. Teague, "Deterministic phase retrieval: a Green's function solution," J. Opt. Soc. Am. **73**, 1434–1441 (1983).
29. T. E. Gureyev, A. Roberts, and K. A. Nugent, "Partially coherent fields, the transport of intensity equation, and phase uniqueness," J. Opt. Soc. Am. A **12**, 1942–1946 (1995).
30. K. Ichikawa, A. W. Lohmann, and M. Takeda, "Phase retrieval based on the irradiance transport equation and the Fourier transform method: experiments," Appl. Opt. **27**, 3433–3436 (1988).
31. D. Paganin and K. A. Nugent, "Noninterferometric phase imaging with partially coherent light," Phys. Rev. Lett. **80**, 2586–2589 (1998).
32. T. E. Gureyev and K. A. Nugent, "Phase retrieval with the transport-of-intensity equation. II. Orthogonal series solution for nonuniform illumination," J. Opt. Soc. Am. A **13**, 1670–1682 (1996); T. E. Gureyev and K. A. Nugent, "Rapid quantitative phase imaging using the transport of intensity equation," Opt. Commun. **133**, 339–346 (1997).
33. A. Barty, K. A. Nugent, D. Paganin, and A. Roberts, "Quantitative optical phase microscopy," Opt. Lett. **23**, 817–819 (1998).
34. See, for example, M. Born and E. Wolf, *Principles of Optics*, corrected 6th ed. (Cambridge U. Press, Cambridge, UK, 1998), pp. 193–194.
35. A. Pogany, D. Gao, and S. W. Wilkins, "Contrast and resolution in imaging with a microfocus x-ray source," Rev. Sci. Instrum. **68**, 2774–2782 (1997).
36. S. Bajt, A. Barty, K. A. Nugent, M. McCartney, M. Wall, and D. Paganin, "Quantitative phase-sensitive imaging in a transmission electron microscope," Ultramicroscopy **83**, 67–73 (2000).
37. I. McNulty, A. Khounsary, Y. P. Feng, Y. Qian, J. Barraza, C. Benson, and D. Shu, "A beamline for 1-4 keV microscopy and coherence experiments at the Advanced Photon Source," Rev. Sci. Instrum. **67**, 3372 (1996).
38. D. Gabor, "A new microscopic principle," Nature (London) **161**, 777–778 (1948).
39. C. Jacobsen, M. Howells, J. Kirz, and S. Rothman, "X-ray holographic microscopy using photoresist," J. Opt. Soc. Am. A **7**, 1847–1861 (1990).
40. J. B. Tiller, A. Barty, D. Paganin, and K. A. Nugent, "The holographic twin image problem: a deterministic phase solution," Opt. Commun. (to be published).
41. See, for example, M. Born and E. Wolf, *Principles of Optics*, corrected 6th ed. (Cambridge U. Press, Cambridge, UK, 1998), pp. 455–458.